

Research Article

Cite this article: Irfan Z, Bashir S, Butt SH, Hayat A, Ayub R, Mahmood K, Akram M, Batool A (2020). Evaluation of electron temperature and electron density of laser-ablated Zr plasma by Langmuir probe characterization and its correlation with surface modifications. *Laser and Particle Beams* **38**, 84–93. <https://doi.org/10.1017/S026303462000004X>

Received: 30 October 2019

Revised: 20 January 2020

Accepted: 6 February 2020


First published online: 16 March 2020

Key words:

Electron number density; electron temperature; Langmuir probe; laser-produced plasma; plasma parameters

Author for correspondence: S. Bashir, Centre for Advanced Studies in Physics, Government College University, Lahore 54000, Pakistan. E-mail: shaziabashir@gcu.edu.pk

Evaluation of electron temperature and electron density of laser-ablated Zr plasma by Langmuir probe characterization and its correlation with surface modifications

Zulaikha Irfan, Shazia Bashir , Shariqa Hassan Butt, Asma Hayat, Rana Ayub, Khaliq Mahmood, Mahreen Akram and Amna Batool

Centre for Advanced Studies in Physics, Government College University, Lahore 54000, Pakistan

Abstract

The plasma parameters of laser-ablated Zirconium (Zr) using a Langmuir probe technique have been investigated by employing a Q-switched Nd:YAG laser (532 nm, 6 ns) at various irradiances ranging from 8.6 to 15.5 GW/cm². All the measurements have been performed under an ultra-high vacuum condition while keeping the probe at a fixed distance of 4 mm from the target. By varying the biasing voltages from 1 to 75 V, the corresponding values of electric currents are measured by the probe on the oscilloscope. Laser-induced Zr plasma parameters such as electron temperature, electron number density, plasma potential, Debye length, and thermal velocity have been evaluated from *I*–*V* characteristic curves of Langmuir probe data. It is found that both the electron temperature and thermal velocity of Zr plasma reveal an increasing trend from 18 to 41 eV and 2.8×10^8 to 4.3×10^8 cm/s, respectively, with increasing laser irradiance which is attributed to more energy deposition and enhanced ablation rate. However, the electron number density of Zr plasma exhibits a non-significant increase from 6.5×10^{14} to 6.7×10^{14} cm⁻³ with increasing irradiance from 8.6 to 10.9 GW/cm². A further increase in irradiance from 12 to 15.5 GW/cm² causes a reduction in the number density of Zr plasma from 6.1×10^{14} to 5.6×10^{14} cm⁻³ which is attributed to the formation of thick sheath, ambipolar electric field, and laser-supported detonation waves (Shock front). Scanning electron microscope analysis has been performed to reveal the surface morphology of irradiated Zr. It reveals the formation of cracks, ridges, cones, and grains. It was observed at high irradiances the ridges are vanished, whereas cones and cracks are dominant features. By controlling plasma parameters, surface structuring of materials can be controlled, which has a vast range of applications in the industry and medicine.

Introduction

Laser ablation of a solid target is a technologically important, simple, and promising technique with a vast range of applications in the field of industry, medicine, and material sciences (Kurella and Dahotre, 2005; Phipps, 2007). The understanding of fundamental mechanisms for the generation, growth, and expansion of laser-produced plasma is a challenging and fascinating field. The plasma with known parameters of kinetic energy and degree of ionization can be successfully employed for various applications, for example, pulse laser deposition of thin film, ion implantation, and micro/nanostructuring of materials (Lippert *et al.*, 1993; Toftmann *et al.*, 2003; Borghesi *et al.*, 2006). The knowledge of electron temperature (T_e) and electron number density (n_e) is highly significant for knowing the dynamics, evolution, and energy deposition mechanisms of laser-generated plasmas.

There are various characterization techniques which can be employed for the evaluation of plasma parameters. The Langmuir probe is one of the simple and promising *in situ* intrusive diagnostic tool used to measure the parameters of plasma (Toftmann *et al.*, 2000; Baraldi *et al.*, 2011). Basically, it consists of merely a small bare wire with well-defined dimensions, which is inserted into the plasma. Charge carriers are collected around a probe and form a well-defined boundary which is called “sheath”, when the applied voltage is swept from a negative to a positive potential. The dimensions of the probe are of great importance, as they play a vital role in the collection of charged particles, that is, length and diameter (Russo *et al.*, 2004; Merlino, 2007). By using the Langmuir probe technique, plasma parameters such as electron temperature, number density, plasma potential, and Debye length can be evaluated from the *I*–*V* characteristic curve. The Langmuir probe characterizations of laser-produced plasmas of various materials are reported by a large number of research groups (Hopkins and Graham, 1986; Donnelly *et al.*, 2010). Dogar *et al.* (2011) studied the temporal behavior of laser-induced Cu plasma and evaluated the plasma parameters at laser irradiance ranging from 4×10^8 to

$13 \times 10^8 \text{ W/cm}^2$. By employing Nd:YAG (1064 nm, 10 ns), the value of the electron temperature, plasma potential, and ion density were, respectively, 3.28 eV, 2.42 V, and $2.3 \times 10^{12} \text{ cm}^{-3}$. Chen *et al.* (2014) reported the UV nanosecond laser ablation of $\text{LaO}_{0.4}\text{CaO}_{0.6}\text{MnO}_3$ in the fluence range of 0.8–1.9 J/cm^2 using both Langmuir probe and mass spectrometry. They observed that with increasing laser fluence, the electron temperature was increased from 0.9 to 1.0 eV and the electron number density was varied from 4×10^{14} to $2 \times 10^{14} \text{ m}^{-3}$. Hendron *et al.* (1997) used the Langmuir probe technique to calculate the plasma potential, electron temperature, and electron number density in the late stages within the time scale of 5 μs of a laser-irradiated Cu plasma. Under vacuum conditions at a fluence of 2.5 J/cm^2 , electron temperature and electron number density were found to be 0.5 eV and 10^{-18} m^{-3} , respectively. Nica *et al.* (2017) used the Langmuir probe technique to characterize the plasma of metallic targets produced by femtosecond laser. The highest value of electron temperature was 14.21 eV for Al and 5.29 eV for W target. Most recently, Nica *et al.* (2019) used the Langmuir probe to measure plasma parameters of Copper and Iron ablated by femtosecond laser irradiation. They studied the influence of external biasing on metallic targets, which can perturb the ambipolar electric field generated through the charge separation at early stages of the expansion.

The motivation of the present research work is to explore the effect of various laser irradiances on the Zirconium (Zr) plasma parameters at 4 mm target to probe distance that how the increasing laser irradiance is translated into the kinetic energy and ionization of Zr plasma with increasing energy deposition. For this purpose, nanosecond Nd:YAG laser (532 nm, 6 ns) was employed for Zr target ablation under ultra-high vacuum (UHV) conditions at various irradiances ranging from 8.6 to 15.5 GW/cm^2 . Within this irradiance range, various research groups have investigated electron temperature and number density in the range of 1.4–16 eV and 10^{12} – 10^{18} cm^{-3} , respectively. They have attributed this increase to the mass ablation rate. The innovative aspect of the present work is the detailed exploration of Zr plasma parameters at a small target to probe distance of 4 mm, which is scarcely reported. No one has correlated the plasma parameter investigation by a Langmuir probe with surface modification after laser ablation.

The effect of laser irradiance on micro/nanostructuring has been studied using the scanning electron microscope (SEM). According to our best knowledge, no work is reported in which the effect of varying irradiance on the plasma parameter measured by a Langmuir probe is correlated with Zr surface structuring. The surface modification of Zr can enhance its optical, thermal, and field emission properties, as well as corrosion and wear resistance, which can highly beneficial for material processing application. The Zr plasma can be used as the best source of electrons and ions for further applications of ion/electron implantation of materials as well as tabletop accelerators.

Experimental details

A schematic of the experimental setup is shown in Figure 1a. Squared shaped Zr samples with a purity of 99.999% were selected as a target material with dimensions of $10 \times 10 \times 5 \text{ mm}^3$. The samples were grinded, polished, and ultrasonically cleaned for 20 min. A Q-switched Nd:YAG (Quantel 981C, France) laser with a wavelength of 532 nm and a pulse duration of 6 ns was employed as an irradiation source to generate Zr plasma. The

prepared Zr targets were placed on the target holder inside a vacuum chamber evacuated to base pressure of 10^{-9} Torr by using a rotary pump followed by a turbo molecular pump. An Nd:YAG laser beam with pulsed energies varying from 150 to 270 mJ, measured by an energy meter (NOVA-QTL; Ophir), was used. The beam after focusing through a focusing lens of the focal length of 50 cm hit the target at an angle of 90° with respect to the target surface and generated the luminous Zr plasma. This plasma was diagnosed with the help of the Langmuir probe technique. The cylindrical Langmuir probe was used for the measurement of plasma parameters, which was consisted of a W wire tip with a diameter of 0.2 mm and a length of 6 mm. The W probe tip was spot welded with a Cu rod of diameter 1.7 mm and a length of 6.1 cm. This Cu rod was insulated with a Teflon rod of diameter 9.9 mm and a length of 17 cm. The whole Teflon rod was drilled according to the copper rod dimensions.

The I - V characteristics of plasma were recorded as a function of laser irradiances by using a Langmuir probe. The Zr target were exposed at seven different laser irradiances of 8.6, 9.8, 10.9, 12.0, 13.2, 14.3, and 15.5 GW/cm^2 corresponding to pulse laser energies of 150, 170, 190, 210, 230, 250, and 270 mJ, respectively. The Langmuir probe biasing voltage was varied from +1 to +75 V, and the electronic signals were determined from the voltage drop across the 1- Ω resistor by means of an oscilloscope having an impedance of 50 Ω . The biasing circuit is shown in Figure 1b. The beam after splitting from the beam splitter entered the photodiode that permit the oscilloscope to trigger. The surface morphology of laser-irradiated Zr target was investigated using an SEM (JEOLL JSM-6480 LV). Zr was exposed to 30 laser pulses at same laser irradiances as have been employed for plasma generation of Zr. Surface modifications were explored from the center and peripheral of ablated regions of targets. When the probe was negatively biased, the electron flow to the probe was suppressed and ions were extracted from the plasma. In our case, at the constant distance of probe to target, that is, 4 mm when the biasing voltage of probe was varied from -1 to -75 V, no ions signals were detected. This might be the oversaturation of ions at such a smaller distance. Therefore, only electron temperature and electron number density of Zr plasma have been evaluated.

Results and discussion

Langmuir probe measurements

Graphs of Figure 2a–2d reveal the temporal evolution of electronic current of Zr plasma at various laser irradiances of (a) 8.6, (b) 10.9, (c) 14.3, and (d) 15.5 GW/cm^2 for fixed biasing voltages of 14, 46, and 62 V. With the increase in laser irradiance from 8.6 to 14.3 GW/cm^2 , the amplitude of electronic signal increases, whereas the temporal delay of the electronic signal reduces from 3 to 1 μs . At the maximum irradiance of 15.5 GW/cm^2 , the amplitude of the current reduces to the value of 2.2 V, and the delay time of species increases up to 3 μs which is also shown graphically in Figure 3 representing the comparison of amplitude of current and delay time of laser-ablated Zr plasma as a function of laser irradiance at the biasing voltage of 46 V. When a nanosecond laser ablation takes place, vaporization of the target starts immediately after the contact of the leading edge of the laser pulse. In addition to the vaporized ionized species, the impact of the trailing part of the laser beam further increases the heating and ionization. The electron temperature of the plasma

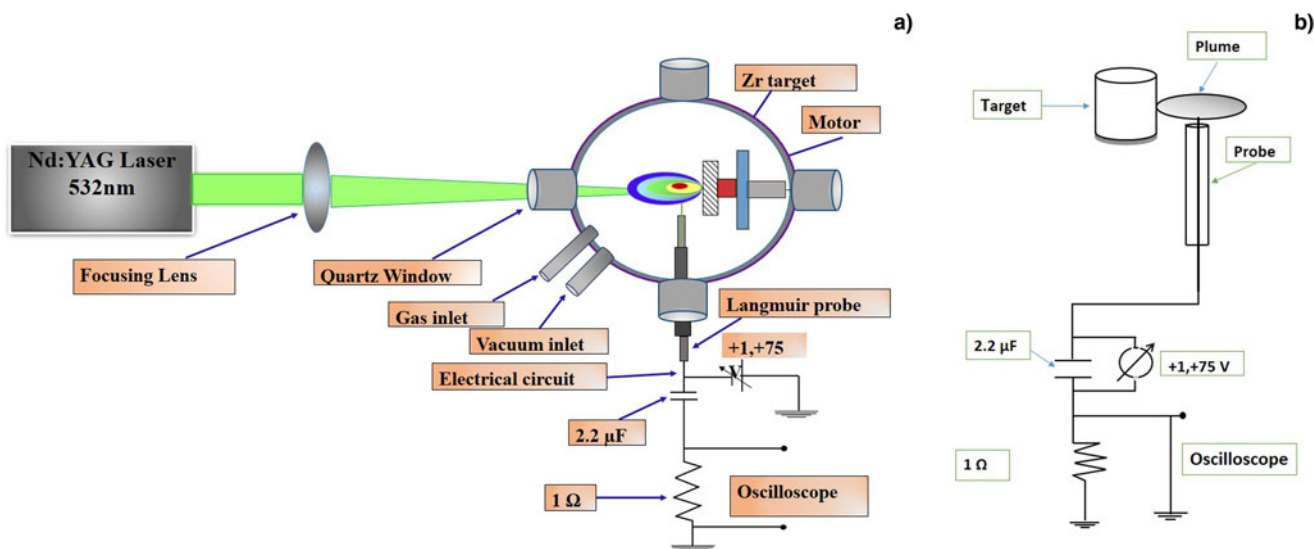


Fig. 1. (a) The schematic of the experimental setup for laser-induced Zr plasma and its diagnostics by a Langmuir probe. (b) The Langmuir probe circuit diagram.

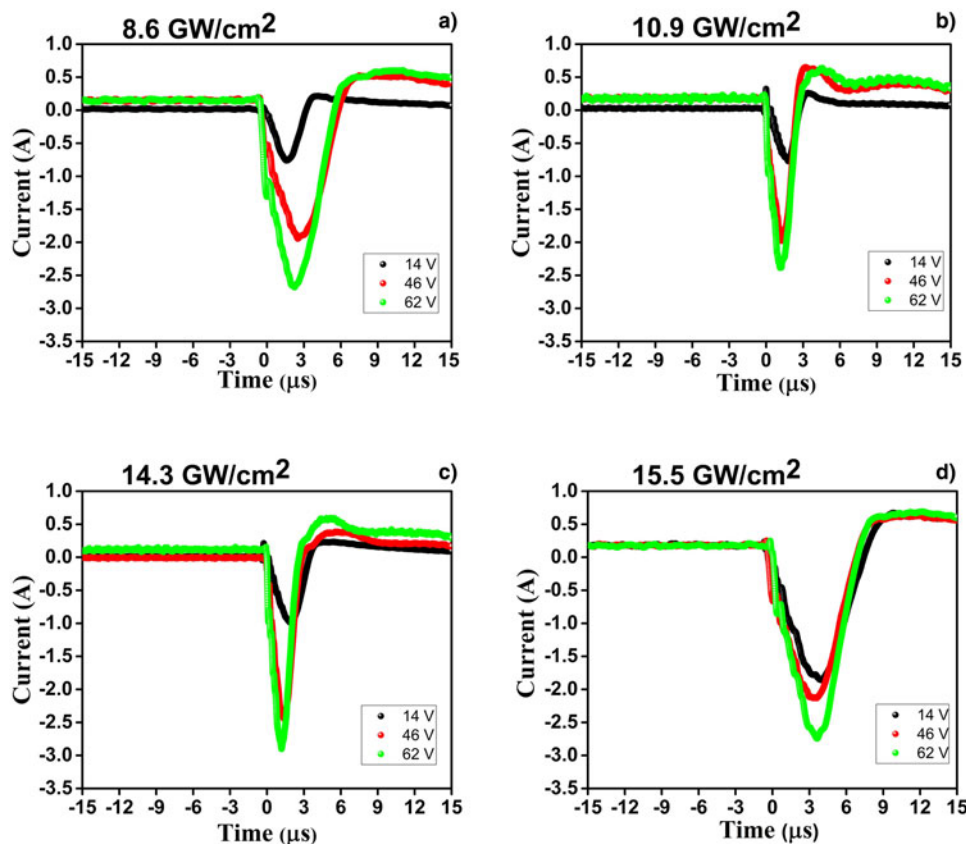


Fig. 2. Temporal evolutions of Langmuir probe signals at 4 mm probe to target distance for Zr plasma at the probe biasing of 14, 46, and 62 V at various laser irradiances of (a) 8.6, (b) 10.9, (c) 14.3, and (d) 15.5 GW/cm².

plume is increased with the increase in laser irradiance (Hafeez *et al.*, 2008a; Rai, 2012). As the ablation rate increases, which, in turn, increases the internal energy of plasma, and as a result, the electron temperature of the species are also increased. Therefore, more energetic electrons reaching the tip of the probe results in an increase in the amplitude of the electronic

signals. At the maximum laser fluence, the decrease in the amplitude of the electronic signal is attributed to more absorption of the laser beam by the shock wave front, enhanced diffusion losses out of focal volume due to enhanced kinetic energies after increased collisional excitation as well as recombination losses (Bashir *et al.*, 2012). Similarly, the kinetic energies and velocity

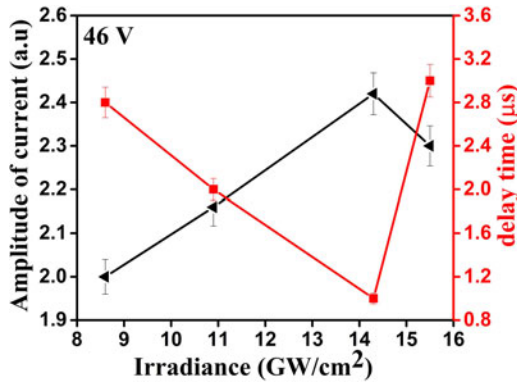


Fig. 3. The comparison of the amplitude of current and delay time of laser-ablated Zr plasma measured by a Langmuir probe as a function of laser irradiance at the biasing voltage of 46 V.

of charged species of the plume are increased by increasing laser irradiance. This will be responsible for reducing the delay time of the electronic signal. Due to the formation of an electric shield around the probe fast-moving electrons are able to overcome this potential in the plasma sheath (Pilling *et al.*, 2003). Graphs of Figure 4a–4d show the typical electronic signal recorded for the various biasing voltages of (a) 14, (b) 36, (c) 46, and (d) 62 V at the laser irradiances of 8.6, 10.9, 14.3, and 15.5 GW/cm², respectively. It is observed that with the increase of biasing voltages from 14 to 46 V, the electronic current increases. However, no decrease in the delay time of the electronic signal is observed. With the increase in the applied potential, the amplitude of the electronic current increases because more electrons are collected toward the probe and flux densities collected by the tip of the probe are increased in terms of peak intensity (Bhatti *et al.*, 2010; Shrestha *et al.*, 2014).

The typical *I*–*V* characteristic curve of the Langmuir probe obtained for Zr plasma is shown in Figure 5a. When positive biasing voltage is applied to the probe, the corresponding electronic current increases due to the collection of more electrons by the tip of the probe. In the *I*–*V* characteristic curve, the region where electrons are attracted by the probe is known as the electron retarding region. The bend is referred to as the “knee” of the curve. At this point, the voltage corresponds to the plasma potential. When the applied potential is greater than this plasma potential, electrons are responsible for the electric shielding of the probe and this region is known as the electron saturation current. Assuming the Maxwellian energy distribution, the current drawn from the probe is given by the following equation (Hafez *et al.*, 2003):

$$I = I_0 \exp\left(\frac{V - V_p}{kT_e}\right), \tag{1}$$

$$\ln\left(\frac{I}{I_0}\right) = \frac{V - V_p}{kT_e}, \tag{2}$$

where *I* is the electronic current, *I*₀ is the electron saturation current, *T*_e is the electron temperature, *k* is the Boltzmann constant, *V*_p is the plasma potential, and *V* is the applied voltage. In the *I*–*V* characteristic curve, the plasma potential (*V*_p) is determined by extrapolating the electron retarding and the saturation region of

the ln[*I*_e]/*V* curve (Hendron *et al.*, 1997), as shown in Figure 4b. The value of the plasma potential increases from 11.4 to 16.8 V with increasing laser irradiances from 8.6 to 15.5 GW/cm².

The typical *I*–*V* characteristic curve of the Langmuir probe obtained for Zr plasma at laser irradiances of 8.6–15.5 GW/cm² is shown in Figure 5b. The biasing voltage is applied to the Langmuir probe from 1 to 75 V. With an increasing biasing voltage up to a value of 15 V, the electronic current increases linearly. A further increase in the biasing voltage is responsible for the saturation of the electronic current. The saturation of the electronic current terminates the exponential behavior which is the typical characterization of a Langmuir probe. It is also observed that the value of collected electron increases for same biasing voltages by increasing the laser irradiance from 8.6 to 13.2 GW/cm². With a further increase of laser irradiance from 14.3 to 15.5 GW/cm², a decrease in the electronic current is observed for same biasing voltage values. The increase in the electronic current curve with increasing the laser irradiances is attributed to enhanced energy deposition to the target surface with higher ablation efficiency. Hence, more energetic species are collected on the probe. At the maximum laser irradiance, the decrease in the electronic current is due to the electron loss which is related to the contributions of recombination, trapping, and diffusion losses (Harilal *et al.*, 1998).

The electron temperature is one of the most important parameters of plasma and is important to understand various dissociation, ionization, and excitation processes (Lacroix *et al.*, 1997). The electron temperature is evaluated from Eq. (1) by using *I*–*V* characteristic curves of the Langmuir probe at various laser irradiances. A graph is plotted between voltage *versus* current, the slope of the straight line in the linear region is 1/*kT*_e, where *T*_e gives the value of electron temperature. Figure 6a shows the variation in electron temperature of Zr plasma with increasing laser irradiance. When laser irradiance increases from 8.6 to 15.5 GW/cm², the electron temperature increases monotonically from 18 to 41 eV. This variation in electron temperature is explainable on the basis of absorption of light during laser-matter interaction. The interaction of laser pulse with the material generates a significant magnitude of the accelerating electric field for the charged particles. The electric field of incoming electromagnetic radiations basically generates the space charge wave in plasma after its interaction with target electrons (Radziemski and Cremers, 1989). The space speed of this wave that is close to the speed of light makes relativistic particles to be accelerated with higher kinetic energies. This peak electric field of the incoming laser beam is related to its irradiance by the relation (Radziemski and Cremers, 1989):

$$E(\text{eV/cm}) = 27\sqrt{I(\text{W/cm}^2)}, \tag{3}$$

where *E* is the electric field, and *I* is irradiance. This electric field increases from 2.5 to 3.3 MeV/cm for minimum to maximum selected irradiance values. The increasing laser irradiance from 8.6 to 15.5 GW/cm² as well as increasing electric field correspond to increasing trend of energy deposition to the Zr target from 56 to 100 eV/atom which is significantly higher than the melting and vaporization threshold of Zr (1 eV). This increasing trend of energy deposition with the increase in irradiance is responsible for the enhanced mass ablation rate of the target which is given

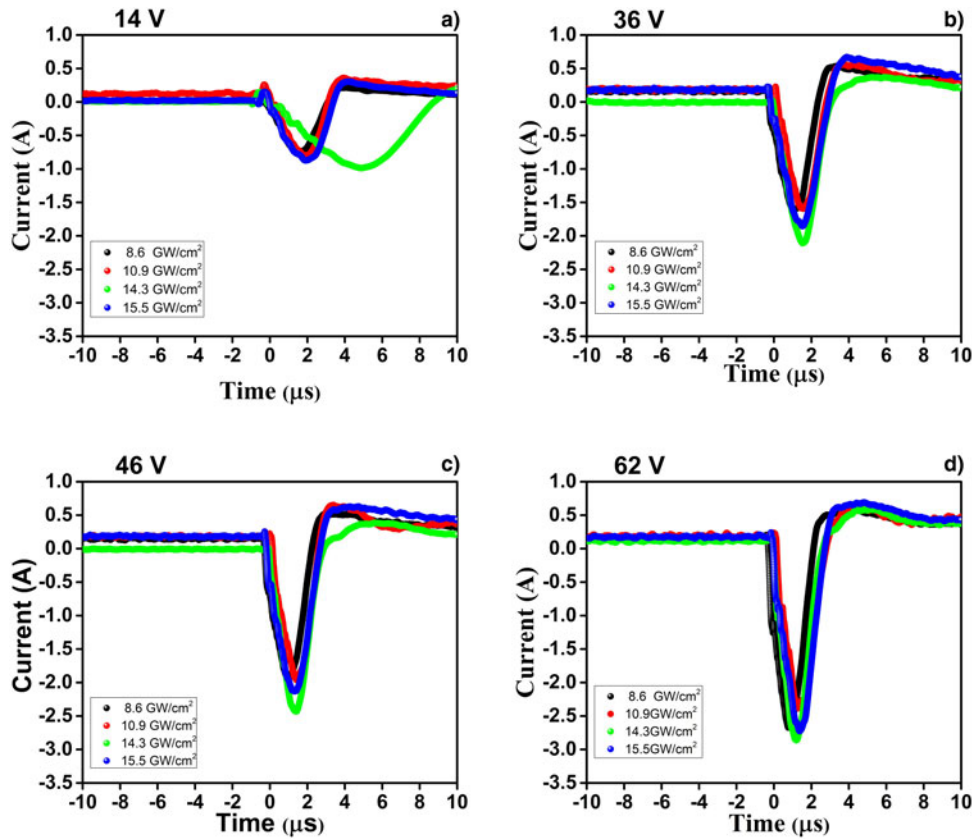


Fig. 4. Temporal evolutions of Langmuir probe signals at 4 mm probe to target distance for Zr plasma at laser irradiances of 8.6, 10.9, 14.3, and 15.5 GW/cm² at various biasing voltages of (a) 14, (b) 36, (c) 46, and (d) 62 V, respectively.

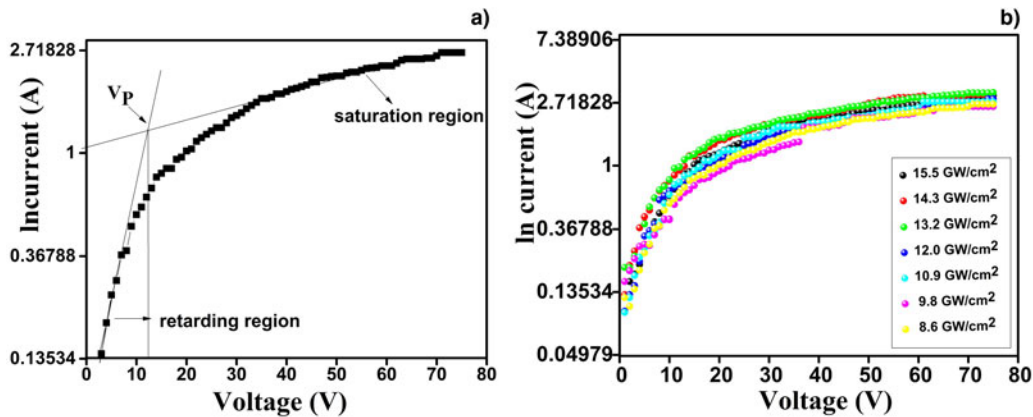


Fig. 5. (a) The *I-V* characteristic curve of the laser-induced Zr plasma with different regions obtained at the irradiance of 8.6 GW/cm². (b) The *I-V* characteristic curve of laser-induced Zr plasma at various laser irradiances of 8.6–15.5 GW/cm².

by the relation as follows (Radziemski and Cremers, 1989):

$$m \text{ (kg/s cm}^2\text{)} = 110 \left(\frac{\varphi_a}{10^{14}} \right) \lambda^{-4/3}, \tag{4}$$

where φ_a is the absorbed fluence, and λ is laser wavelength. In the present case, the analytical value of the mass ablation rate of Zr increases from 1.13×10^{-3} to 1.36×10^{-3} (kg/s cm²) with the increase of irradiance ranging from 8.6 to 15.5 GW/cm², respectively. These considerable effects finally result in an increase of

electron temperature of Zr plasma at higher irradiances (Hafeez et al., 2008b).

The electron thermal velocity is calculated by the following expression (Hendron et al., 1997):

$$v = \sqrt{\frac{8kT_e}{\pi m_e}}, \tag{5}$$

where k is the Boltzmann constant, T_e is the electron temperature, and m_e is the mass of an electron. Figure 6b shows the variation in

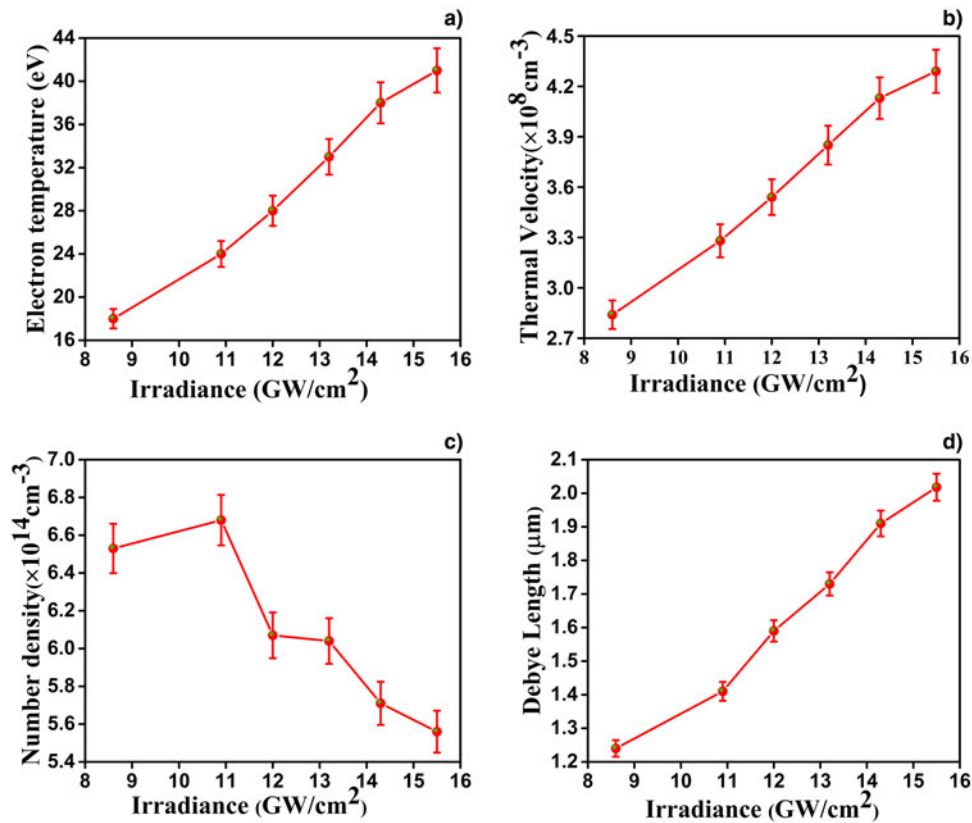


Fig. 6. The variations in (a) electron temperature, (b) thermal velocity, (c) electron number density, and (d) Debye length of Zr plasma as a function of laser irradiance ranging from 8.6 to 15.5 GW/cm².

electron thermal velocity variation with the increasing laser irradiance from 8.6 to 15.5 GW/cm². The electron velocity increases from 2.8×10^8 to 4.3×10^8 cm/s by increasing the laser irradiances from 8.6 to 15.5 GW/cm². A dense plasma absorbs strongly the trailing part of the laser pulse. The absorption of the laser radiation by the plasma increases the velocity of the species. During this process, plasma thermal energy is converted into the translation energy of the species which is responsible for the enhancement of electron thermal velocity. The particle acceleration depends upon the initial temperature and the mass of the species produce in this expansion (Singh and Narayan, 1990; Kumari and Khare, 2014).

The electron saturation current is proportional to electron density (n_e) and is expressed by the following relationship (Doggett and Lunney, 2009):

$$I_0 = \frac{1}{4} e v_e A n_e, \tag{6}$$

where I_0 is the electron saturation current, e is the electronic charge, v_e is the thermal velocity of electrons, A is the area of the probe, and n_e is the number density of electrons.

Figure 6c shows that initially with the increasing laser irradiance from 8.6 to 10.9 GW/cm², electron density increases from 6.5×10^{14} to 6.7×10^{14} cm⁻³. Initially with the increase in laser irradiance, number density increases. This increase is attributed to enhanced ablation rate, collisional frequency of neutrals with ions. However, a further increase in laser irradiance from 10.9 to 15.5 GW/cm² causes a decrease in number density, in spite of fact electron temperature increases monotonically in this

region. This decrease in number density with the increase in laser irradiance is explainable on the basis of the ambipolar electric field (double layer) generated in the ablated plume of Zr plasma. The condition for the formation of the ambipolar electric field is $a \gg \lambda_D$ (Radziemski and Cremers, 1989), where a is beam radius, and λ_D denotes Debye length. The value of the laser beam radius is 0.96 mm, which is much higher than λ_D ranges from 1.2 to 2 μm. This mechanism suggests that in early times of the plume expansion, the electron being the lighter particle as compared to the ion moves faster, thus leaving behind the positive cloud. According to the Gauss law, an electric potential V_0 (also known as the ambipolar electric field) is generated (Radziemski and Cremers, 1989). This electric potential accelerates the ions and plays the role of potential barrier for further incoming electrons (Radziemski and Cremers, 1989). Only the high energy electrons have the ability to cross the barrier, whereas the low energy electrons could not reach the probe surface. Thus, the formation of an additional electric field within a Debye length is responsible for the decrease in number density. Moreover, the value of electric field increases with the increase in laser irradiance. Another possible reason for the decrease in number density is the formation of thick sheath around the Langmuir probe at higher laser irradiance. When the probe is positively biased electron shielding cloud surrounding it starts to attract the ions from plasma and hinders the further electrons motion toward the probe (Torrizi and Gammino, 2006). With the increase in laser irradiance, the sheath becomes more and more thick, and as a result, a less number of electrons are able to reach the probe, thus decreasing the number density. Moreover, the electron density is inversely proportional to the square root of electron velocity as given in Eq. (6).

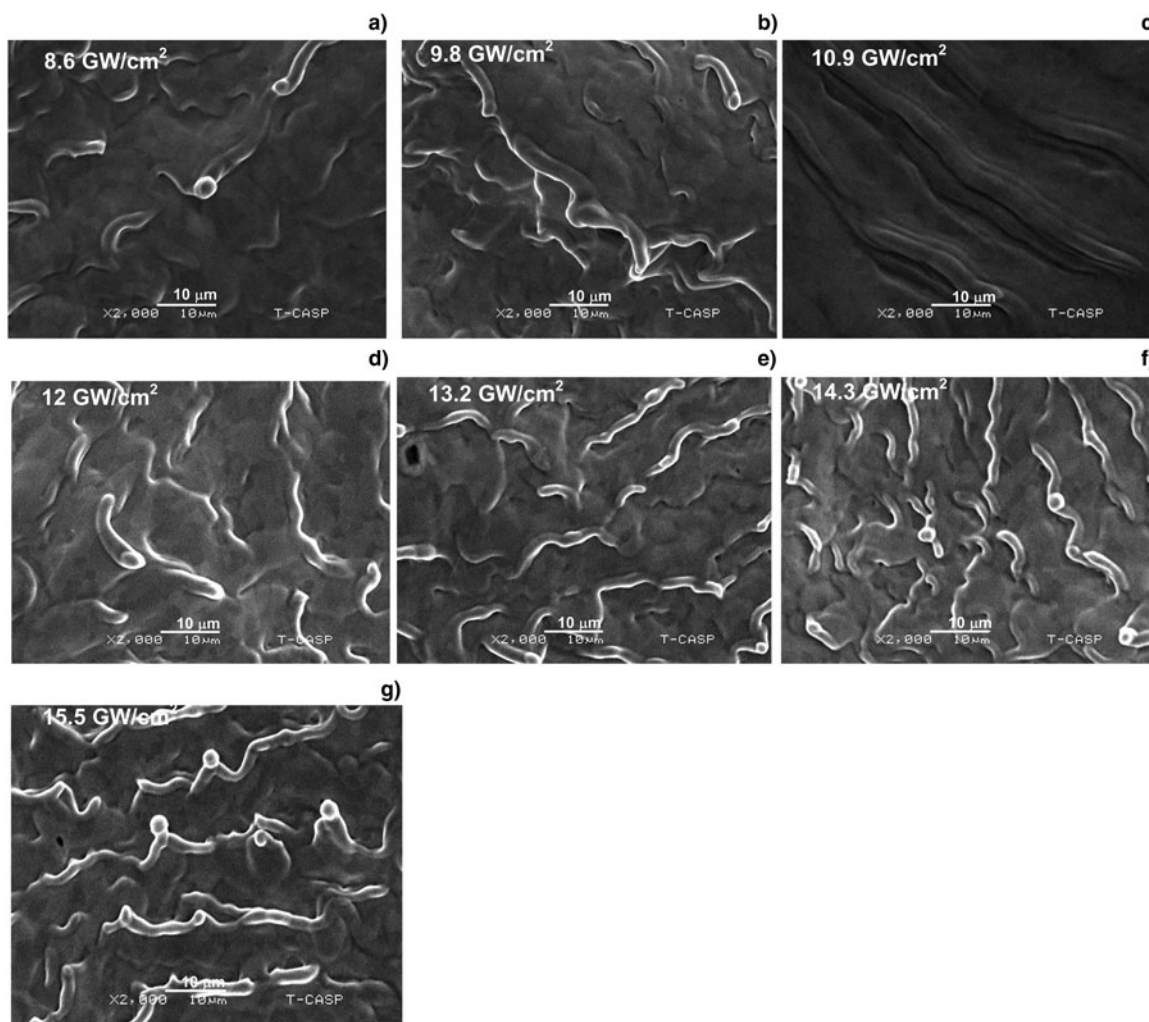


Fig. 7. SEM analysis exhibiting the surface morphology of central ablated area of laser-irradiated Zr under UHV at different laser irradiances of (a) 8.6, (b) 9.8, (c) 10.9, (d) 12.0, (e) 13.2, (f) 14.3, and (g) 15.5 GW/cm².

With the increasing laser irradiance, electron velocity increases and correspondingly the number density of Zr plasma decreases. The other possible mechanism for density decrease is also attributed to the absorption of laser beam by laser-supported detonation waves (Shock front) (Radziemski and Cremers, 1989). These shock waves will reduce the intensity of laser beam which reaches the target surface.

Graph of Figure 6d shows the effect of laser irradiance on the Debye length with the increasing laser irradiance from 8.6 to 15.5 GW/cm². The Debye length increases from 1.2 to 2.0 μm by increasing laser irradiances from 8.6 to 15.5 GW/cm². The collection of the electronic current increases due to the increase in the biasing voltage from 1 to 75 V, but at one point, the incoming electrons are repelled by the probe due to the formation of electronic cloud named as “sheath” (Lai et al., 1993). This electronic cloud will limit the penetration of the external electric field into the plasma maintained at a distance approximately to electron Debye length λ_D , which is written as follows (Bhatti et al., 2010):

$$\lambda_D = \sqrt{\frac{\epsilon_0 k T_e}{e^2 n_e}}, \quad (7)$$

where ϵ_0 is the permittivity of free space, k is the Boltzmann constant, T_e is the electron temperature, e is the electronic charge, and n_e is the electron number density. For high-density plasma, the sheath width is small ≤ 0.1 mm. Therefore, the expansion in the sheath produces a negligible increase in the electronic current as the probe bias is increased. If the density is lower and the area of the probe is small, the collected current increases as the expansion in the sheath increases, because the collection of the particles is around the sheath area and not the area of geometry (Merlino, 2007).

Effect of laser irradiance on the surface morphology of laser-ablated Zr explored by SEM analysis

When a high-intensity laser is used to irradiate the sample surface, the bound potential of free electrons is distorted by the electric field of the laser parallel to the surface normal. This distortion of potential induces tunneling photoelectron ejection from the metal surface via multiphoton absorption. Therefore, in order to correlate the electron emission with the threshold fluence of ablated material, simply the ionization potential and work function cannot define ablation threshold for the material, and it is highly important to find out the ablation threshold by a

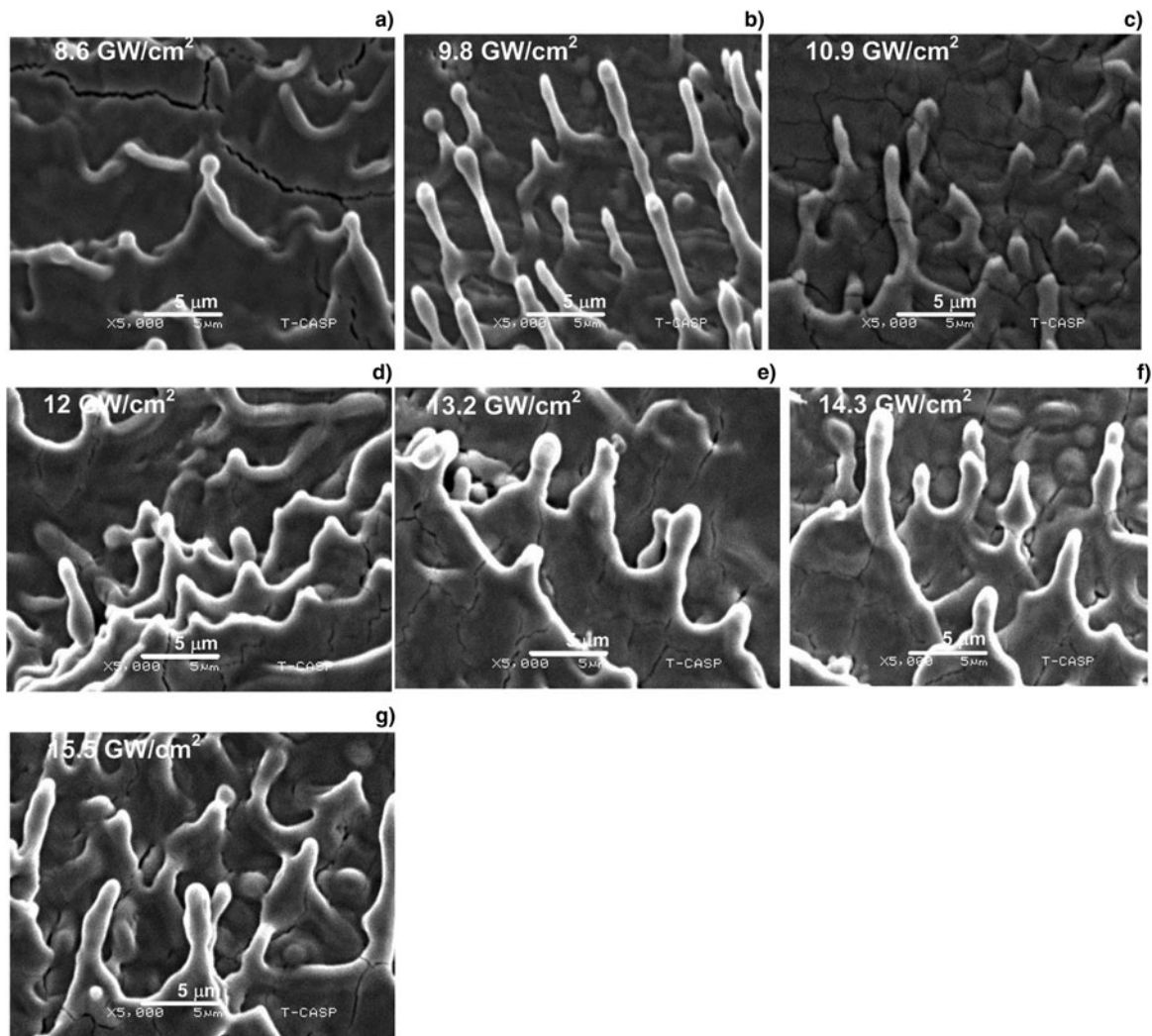


Fig. 8. SEM images revealing the surface morphology of peripheral ablated area of laser-irradiated Zr under UHV at different laser irradiances of (a) 8.6, (b) 9.8, (c) 10.9, (d) 12.0, (e) 13.2, (f) 14.3, and (g) 15.5 GW/cm².

surface-ablated area which justifies SEM analysis of laser-ablated Zr. For this reason, SEM has been performed to reveal the surface morphology of Zr after ablation at various laser irradiances ranging from 8.6 to 15.5 GW/cm².

The surface modifications of laser-ablated Zr were explored by SEM analysis. The Zr targets were exposed to 30 laser shots at same laser irradiances which have been employed for plasma generation of Zr during Langmuir characterization. The plasma impact on the overall phenomenon of laser-matter interaction and its particular features such as the influence of excited plasma reradiation, back flux of energetic plasma species, and massive material redeposition on surface quality and processing efficiency is highly important.

SEM images of Figure 7 reveal the variation in the surface morphology of the peripheral ablated regions of the Zr targets under UHV conditions for various laser irradiances of (a) 8.7, (b) 9.8, (c) 10.9, (d) 12, (e) 13.2, (f) 14.3, and (g) 15.5 GW/cm². Various features like periodic surface structure (ripples), ridges, highly uplifted protruding cones, cracks, and grains are dominant characteristics, which are observed on the surface of irradiated Zr and are found to be dependent upon the laser irradiances. Figure 7a shows the diffusive ripples with the protruding

cap-like structure for the lowest irradiance of 8.6 GW/cm². For the irradiance of 9.8–12 GW/cm², embedded ripples are seen in Figure 7b–7d. In Figure 7e, at the irradiance of 13.2 GW/cm², the formation of ripples with diffusive ridges is observed. With the further enhancement of irradiance up to 14.3 GW/cm², these ripples become more pronounced as shown in Figure 7f. Ridges with the protruding conical structure are observed at the maximum irradiance of 15.5 GW/cm² in Figure 7g. Laser Induced Periodic Structures (LIPS) are described on the basis of theories such as the generation of surface plasmon polaritons (Das *et al.*, 2013), Kelvin–Helmholtz instability (Ang *et al.*, 1998), and capillary waves (Shen *et al.*, 2003). The formation of ripples in the present case is attributed to the plasma instabilities like Kelvin–Helmholtz instabilities. According to this theory, the ripple formation is caused by the fast heating and melting of the surface layer and the formation of laser-induced surface waves. The splashing, redeposition, solidification, and permanent engraving of the ablated material in the laser-induced surface layer finally cause the formation of micro ripples (Kawakami and Ozawa, 2003; Barmina *et al.*, 2009). At the maximum irradiance of 15.5 GW/cm², distinctness of ripples increases and they become more organized due to higher values of T_c as calculated

by Langmuir probe measurements. SEM images of Figure 8a reveal the surface morphology of irradiated Zr at the lowest irradiance of 8.6 GW/cm^2 . The formation of ridges with wide base, small heighted cones and cracks are seen at the surface. The ridges are formed when the recoil pressure exerted by the plasma is enhanced which causes the more splashing of material toward the boundary (Yu and Lu, 1999), whereas the presence of thermal stresses on the surface is the possible reason for the crack formation (Kalsoom *et al.*, 2013). With increasing the irradiances from 8.6 to 9.8 GW/cm^2 in Figure 8b, these ridges are completely vanished along with the appearance of distinct and uplifted cones. The growth of such a conical structure is explainable into two stages: in the first stage, the pressure which is exerted by the laser irradiation on the target surface generates stresses as well as depression which are responsible for their growth (Khalid *et al.*, 2016). In the next step, the relaxation of these stresses after terminating of the laser pulse causes the evolution of the conical structures (Khalid *et al.*, 2016). At the irradiance of 10.9 GW/cm^2 of Figure 8c, the surface morphology shows an increase in the density of the cracks, whereas density, height, and distinctness of the protruding cones are reduced significantly. Figure 8d reveals that the density and size of the cracks are decreased, and only few cones are seen as the irradiance is increased up to 12 GW/cm^2 . This decrease in density and size of cracks is due to the refilling of cracks due to splashing and melt displacement. Further enhancement of irradiance from 12 to 13.2 GW/cm^2 in Figure 8e, the distinctness and elevation of ridges are increased. On increasing the irradiance further up to 14.3 GW/cm^2 of Figure 8f, the heighted cones with wider bases are observed that is attributed to more energy deposition to the target surface and the more melting on the target surface. The measured height of the cone is 2.5 to $5.2 \mu\text{m}$. The grain growth is also seen in the ablated regions. The reason for the generation of the residual stresses on the target surface due to the fast heating and cooling results in the high-temperature gradients. This localized heating and cooling is the cause of the grain-like morphology (Mahmood *et al.*, 2010). In Figure 8g, for the highest irradiance of 15.5 GW/cm^2 , the unorganized cones along with cracking are also seen on the surface. Melting and recrystallization of metal along with maximum electron temperature deposited to lattice in the laser-irradiated area are the possible cause for this grain-like structure morphology (Shazia *et al.*, 2015).

Above observations suggest that laser irradiance plays an effective role for plasma parameters as well as the surface modification of Zr. By controlling the plasma parameters, we can control the growth of different structures. When the energy deposition increases, electron temperature increases and is responsible for the growth of more pronounced ripples on the center of the ablated region, whereas uplifted cones and ridges at the periphery region are observed. With an increase of laser irradiance, electron temperature increases, hence the distinctness of the ripples increases.

Conclusions

The Langmuir probe is used as a diagnostic tool to investigate plasma parameters after laser ablation of Zr target under the UHV condition. Both the electron temperature and electron density of Zr plasma are strongly dependent upon the laser irradiance. The electron temperature increases from 18 to 41 eV with the increasing laser irradiance from 8.6 to 15.5 GW/cm^2 . Whereas electron number density increases from 6.5 to

6.7 cm^{-3} , with the increasing irradiance ranges from 8.6 to 10.9 GW/cm^2 and then decreases from 6.1 to 5.6 cm^{-3} . Both the thermal velocity and Debye length increases from 2.8×10^8 to $4.3 \times 10^8 \text{ cm/s}$ and 1.2 to $2.0 \mu\text{m}$, respectively. The plasma potential is also found to increase with the electron temperature.

The significant effect of various laser irradiances on the surface morphology of ablated Zr has been revealed by an SEM. SEM investigation revealed the formation of various structure ripples, cracks, grains, and cones on the center and outer boundary of the ablated region. The growth of these features is also dependent upon plasma parameters as well as the laser energy deposition. The structured Zr is highly useful for the enhancement of optical, mechanical, frictional, and field emission properties and can be become more suitable for device fabrication and in various medical and industrial applications. Therefore, the knowledge of plasma parameters is highly important. By controlling plasma parameters, the formation and growth of various surface structures can be controlled, for example by increasing the electron/ion temperature, the periodic surface structure become more organized and distinct.

References

- Ang L, Lau Y, Gilgenbach R, Spindler H, Lash J and Kovaleski S (1998) Surface instability of multipulse laser ablation on a metallic target. *Journal of Applied Physics* **83**, 4466–4471.
- Baraldi G, Perea A and Afonso CN (2011) Dynamics of ions produced by laser ablation of several metals at 193 nm. *Journal of Applied Physics* **109**, 043302.
- Barmina EV, Barberoglu M, Zorba V, Simakin AV, Stratakis E, Fotakis K and Shafeev GA (2009) Surface nanotexturing of tantalum by laser ablation in water. *Quantum Electronics* **39**, 89–93.
- Bashir S, Farid N, Mahmood K and Rafique MS (2012) Influence of ambient gas and its pressure on the laser-induced breakdown spectroscopy and the surface morphology of laser-ablated Cd. *Applied Physics A* **107**, 203–212.
- Bhatti KA, Khaleeq-ur-Rahman M, Rafique MS, Chaudhary KT and Latif A (2010) Electrons emission from laser induced metallic plasmas. *Vacuum* **84**, 980–985.
- Borghesi M, Fuchs J, Bulanov SV, MacKinnon AJ, Patel PK and Roth M (2006) Fast ion generation by high-intensity laser irradiation of solid targets and applications. *Fusion Science and Technology* **49**, 412–439.
- Chen J, Lunney JG, Lippert T, Ojeda-G-P A, Stender D, Schneider CW and Wokaun A (2014) Langmuir probe measurements and mass spectrometry of plasma plumes generated by laser ablation of $\text{La}_{0.4}\text{Ca}_{0.6}\text{MnO}_3$. *Journal of Applied Physics* **116**, 073303.
- Das SK, Khan MMR, Parandhaman T, Laffir F, Guha AK, Sekaran G and Mandal AB (2013) Nano-silica fabricated with silver nanoparticles: anti-fouling adsorbent for efficient dye removal, effective water disinfection and biofouling control. *Nanoscale* **5**, 5549–5560.
- Dogar AH, Ilyas B, Ullah S, Nadeem A and Qayyum A (2011) Langmuir probe measurements of Nd:YAG laser-produced copper plasmas. *IEEE Transactions on Plasma Science* **39**, 897–900.
- Doggett B and Lunney JG (2009) Langmuir probe characterization of laser ablation plasmas. *Journal of Applied Physics* **105**, 033306.
- Donnelly T, Lunney JG, Amoroso S, Bruzzese R, Wang X and Ni X (2010) Dynamics of the plumes produced by ultrafast laser ablation of metals. *Journal of Applied Physics* **108**, 043309.
- Hafeez S, Shaikh NM and Baig MA (2008a) Spectroscopic studies of Ca plasma generated by the fundamental, second, and third harmonics of a Nd:YAG laser. *Laser and Particle Beams* **26**, 41–50.
- Hafeez S, Shaikh NM, Rashid B and Baig MA (2008b) Plasma properties of laser-ablated strontium target. *Journal of Applied Physics* **103**, 083117.
- Hafez MA, Khedr MA, Elaksher FF and Gamal YE (2003) Characteristics of Cu plasma produced by a laser interaction with a solid target. *Plasma Sources Science and Technology* **12**, 185–198.

- Harilal SS, Bindhu CV, Nampoori VPN and Vallabhan CPG** (1998) Temporal and spatial behavior of electron density and temperature in a laser-produced plasma from $\text{YBa}_2\text{Cu}_3\text{O}_7$. *Applied Spectroscopy* **52**, 449–455.
- Hendron JM, Mahony CMO, Morrow T and Graham WG** (1997) Langmuir probe measurements of plasma parameters in the late stages of a laser ablated plume. *Journal of Applied Physics* **81**, 2131–2134.
- Hopkins M and Graham W** (1986) Langmuir probe technique for plasma parameter measurement in a medium density discharge. *Review of Scientific Instruments* **57**, 2210–2217.
- Kalsoom U-i, Bashir S and Ali N** (2013) SEM, AFM, EDX and XRD analysis of laser ablated Ti in nonreactive and reactive ambient environments. *Surface and Coatings Technology* **235**, 297–302.
- Kawakami Y and Ozawa E** (2003) Tungsten microcone growth by laser irradiation. *Applied Surface Science* **218**, 176–188.
- Khalid A, Bashir S, Jalil SA, Akram M, Hayat A and Dawood A** (2016) Spectroscopic and morphological studies of laser ablated silver. *Optik* **127**, 5128–5134.
- Kumari S and Khare A** (2014) Langmuir probe studies of laser ablated ruby plasma and correlation with pulsed laser deposited ruby thin film properties. *Laser and Particle Beams* **32**, 359–367.
- Kurella A and Dahotre N** (2005) Review paper: Surface modification for bio-implants: The role of laser surface engineering. *Journal of Biomaterials Applications* **20**, 5–50.
- Lacroix D, Jeandel G and Boudot C** (1997) Spectroscopic characterization of laser-induced plasma created during welding with a pulsed Nd:YAG laser. *Journal of Applied Physics* **81**, 6599–6606.
- Lai C, Breun RA, Sandstrom PW, Wendt AE, Hershkowitz N and Woods RC** (1993) Langmuir probe measurements of electron temperature and density scaling in multidipole radio frequency plasmas. *Journal of Vacuum Science and Technology A* **11**, 1199–1205.
- Lippert T, Stebani J, Ihlemann J, Nuyken O and Wokaun A** (1993) Excimer laser ablation of novel triazine polymers: influence of structural parameters on the ablation characteristics. *The Journal of Physical Chemistry* **97**, 12296–12301.
- Mahmood K, Farid N, Ghauri IM, Afzal N, Idrees Y and Mubarak FE** (2010) Effects of laser irradiation on the mechanical response of polycrystalline titanium. *Physica Scripta* **82**, 045606.
- Merlino RL** (2007) Understanding Langmuir probe current-voltage characteristics. *American Journal of Physics* **75**, 1078–1085.
- Nica P, Gurlui S, Osiac M, Agop M, Ziskind M and Focsa C** (2017) Investigation of femtosecond laser-produced plasma from various metallic targets using the Langmuir probe characteristic. *Physics of Plasmas* **24**, 103119.
- Nica PS, Gurluib M and Agopa C** (2019) Oscillatory regimes of Langmuir probe current in femtosecond laser-produced plasmas: Experimental and theoretical investigations. *Applied Surface Science* **481**, 125–132.
- Phipps C** (2007) *Laser Ablation and its Applications*, Vol. **129**. Springer, doi: [10.1007/978-0-387-30453-3](https://doi.org/10.1007/978-0-387-30453-3).
- Pilling LS, Bydder EL and Carnegie DA** (2003) A computerized Langmuir probe system. *Review of Scientific Instruments* **74**, 3341–3346.
- Radziemski LJ and Cremers DA** (1989) *Laser-Induced Plasmas and Applications*, Vol. **21**. CRC Press. ISBN: 0824780787, 9780824780784.
- Rai V** (2012) Theoretical aspect of enhancement and saturation in emission from laser produced plasma. *Laser and Particle Beams* **30**, 621–631.
- Russo RE, Mao XL, Liu C and Gonzalez J** (2004) Laser assisted plasma spectrochemistry: laser ablation. *Journal of Analytical Atomic Spectrometry* **19**, 1084–1089.
- Shazia B, Shazaib K, Mahreen A, Nisar A, Umm-i K, Shahbaz A and Daniel Y** (2015) Pulsed laser ablation of Ni in vacuum and N_2 atmosphere at various fluences. *Quantum Electronics* **45**, 640–647.
- Shen M, Crouch C, Carey J, Younkin R, Mazur E, Sheehy M and Friend C** (2003) Formation of regular arrays of silicon microspikes by femtosecond laser irradiation through a mask. *Applied Physics Letters* **82**, 1715–1717.
- Shrestha A, Shrestha R, Baniya H, Tyata R, Subedi D and Wong C** (2014) Influence of discharge voltage and pressure on the plasma parameters in a low pressure DC glow discharge. *International Journal of Recent Research and Review* **VII**, 9–15. ISSN 2277-8322.
- Singh RK and Narayan J** (1990) Pulsed-laser evaporation technique for deposition of thin films: physics and theoretical model. *Physical Review B* **41**, 8843.
- Toftmann B, Schou J, Hansen TN and Lunney JG** (2000) Angular distribution of electron temperature and density in a laser-ablation plume. *Physical Review Letters* **84**, 3998–4001.
- Toftmann B, Schou J and Lunney JG** (2003) Dynamics of the plume produced by nanosecond ultraviolet laser ablation of metals. *Physical Review B* **67**, 104101.
- Torrisi L and Gammino S** (2006) Method for the calculation of electrical field in laser-generated plasma for ion stream production. *Review of Scientific Instruments* **77**, 03B707.
- Yu JJ and Lu YF** (1999) Laser-induced ripple structures on Ni–P substrates. *Applied Surface Science* **148**, 248–252.